

www.acsami.org Research Article

Magnetic and Optical Properties of Au—Co Solid Solution and Phase-Separated Thin Films and Nanoparticles

David A. Garfinkel, Nan Tang, Grace Pakeltis, Reece Emery, Ilia N. Ivanov, Dustin A. Gilbert, and Philip D. Rack*



Cite This: ACS Appl. Mater. Interfaces 2022, 14, 15047–15058



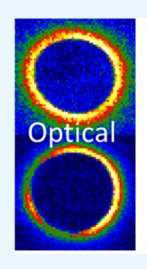
ACCESS

Metrics & More

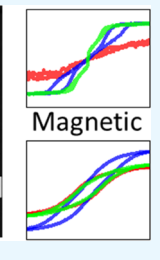


SI Supporting Information

ABSTRACT: The chemical composition and morphology of $\operatorname{Au_xCo_{1-x}}$ thin films and nanoparticles are controlled via a combination of cosputtering, pulsed laser-induced dewetting (PLiD), and annealing, leading to tunable magnetic and optical properties. Regardless of chemical composition, the as-deposited thin films and as-PLiD nanoparticles are found to possess a face-centered cubic (FCC) $\operatorname{Au_xCo_{1-x}}$ solid-solution crystal structure. Annealing results in large phase-separated grains of Au and Co in both the thin films and nanostructures for all chemical compositions. The magnetic and optical properties are characterized via vibrating sample magnetometry (VSM), ellipsometry, optical transmission spectroscopy, and electron energy loss spectroscopy







(EELS). Despite the exceptionally high magnetic anisotropy inherent to Co, the presence of sufficient Au (72 atom %) in the Au_xCo_{1-x} solid solution results in superparamagnetic thin films. Among the as-PLiD nanoparticle samples, an increased Co composition leads to a departure from traditional ferromagnetism in favor of wasp-waisted hysteresis caused by magnetic vortices. Phase separation resulting from annealing leads to ferromagnetism for all compositions in both the thin films and nanoparticles. The optical properties of Au_xCo_{1-x} nanostructures are also largely influenced by the chemical morphology, where the Au_xCo_{1-x} intermixed solid solution has significantly damped plasmonic performance relative to pure Au and comparable to pure Co. Phase separation greatly enhances the quality factor, optical absorption, and electron energy loss spectroscopy (EELS) signatures. The enhancement of the localized surface plasmon resonances (LSPRs) scales with the reduction in Co composition, despite EELS evidence that excitation of the Co portions of a nanoparticle can provide a similar, and in some instances enhanced, LSPR resonance compared to Au. This behavior, however, is seemingly limited to the LSPR dipole mode, while higher-order modes are greatly damped by a Co aloof position. This observed magneto-plasmonic functionality and tunability could be applicable in biomedicine, namely, cancer therapeutics.

KEYWORDS: magnetic, optical, plasmonic, nanoparticles, solid solution, phase separation

■ INTRODUCTION

Alloying in metallic nanomaterials is a powerful means to not only control a specific material property but also to create multiple functionalities, e.g., simultaneous magnetic and plasmonic properties. When introducing additional components to a material system, factors such as chemical composition, mixing behavior, and changes to equilibrium crystal structure can all have a profound influence on the resultant material properties. Combinatorial sputtering provides a convenient tool for rapidly achieving thin-film nanomaterials over a large compositional range. 1,2 Further, the high-energy deposition process and fast cooling rates allow for the realization of metastable material configurations, for example, the as-deposited supersaturated solid solution found in various sputtered alloys.²⁻⁴ Subsequent annealing can be used to achieve the equilibrium thermodynamic state of the system through recrystallization, grain growth, and phase separation.

High-temperature heat treatments can also be used to alter the physical morphology of the thin metallic films through a process called dewetting. The exceptionally high surface energy inherent to thin films, due to the large ratio of surface area to volume, renders the as-deposited thin films metastable. The energetically stable configuration is an array of spherical caps with wetting angles and diameters dependent on the substrate/material properties and thin-film thickness. Timescales to reach this state at room temperature are exceedingly long, and thus thin films maintain their shape at room temperature for extended periods of time. The introduction of heat greatly accelerates the dewetting dynamics and can shorten the duration to nanoseconds when ultrathin films liquify. The use of a pulsed laser to generate these arrays of nanoparticles is termed pulsed laser-induced dewetting (PLiD): a review on

Received: February 1, 2022 Accepted: March 15, 2022 Published: March 25, 2022





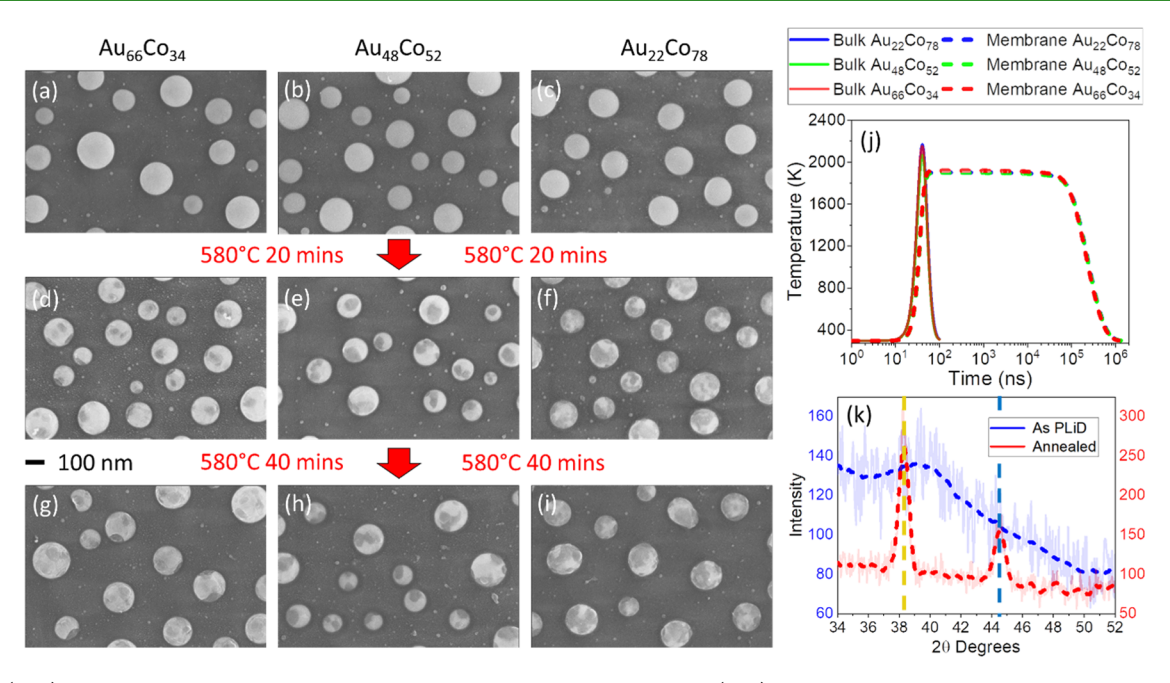


Figure 1. (a–c) Nanoparticles synthesized via PLiD with three different compositions, (d–f) PLiD nanoparticles following 20 min of annealing at 580 °C, (g–i) PLiD nanoparticles following 60 min of annealing at 580 °C, (j) thermal simulations of a single laser pulse with thick Si (solid line) and thin SiN_x (dashed line) substrates for the three 10 nm thin films, and (k) XRD measurements on the Au₅₀Co₅₀ as-PLiD and 20 min annealed samples. The gold dashed line indicates the position of the Au (111) peak, and the blue dashed line indicates the position of the overlapping Au (200) and Co (111) peaks.

the hydrodynamics can be found here. $^{5-8}$ The rapid processing time associated with this technique can also create metastable configurations that can be altered with annealing. PLiD thus offers another option for the production of functional metallic nanoparticles in addition to the various synthesis techniques that are commonly used. $^{9-12}$

Nanomaterials possessing combined magnetic and plasmonic properties have recently emerged as enticing functional materials in various applications including cancer detection and treatment, 13-16 magnetic resonance imaging, 17,18 data storage, 19 and mechanochromic devices. 20 These properties are predominantly achieved with nanoparticles in the Fe_{3-r}O₄ material system, though Au-Co also demonstrates this bifunctionality, in addition to attractive catalyst capabilities. 21,22 The majority of research on Au-Co nanoparticles has been focused on nanoparticles achieved via chemical growth techniques; 23-25 recently, functional Au-Co nanoparticles have also been achieved through laser ablation. 26,27 Research in the thin-film configuration have been studied as multilayers for data storage, ¹⁹ and mixed as-deposited thin films, via evaporation ^{28–30} and sputtering ^{31–33} with much of the focus on the material structure, ^{29,31} which has been observed as a solid solution, amorphous, and a solid solution with interspersed Au and Co particles.

In previous work, we have demonstrated magnetron radio frequency sputtering and PLiD as a robust technique for the synthesis of magneto-plasmonic bifunctionality.³⁴ The size of as-deposited Ag₅₀Ni₅₀ thin films and PLiD nanoparticles provided a tunable parameter for the magnetic and plasmonic properties, namely, exhibiting control in LSPR resonance frequency and superparamagnetic blocking temperature. Here, we expand this research in a new material system, Au_xCo_{1-x}, by examining the influence of composition and chemical morphology on the material properties. The as-deposited thin film and as-PLiD nanoparticles are compared with phase-

separated thin films and nanoparticles at multiple compositions within a large compositional range. Further, electron beam lithography is used to synthesize as-deposited and annealed rod shapes for improved optical response and more straightforward characterization of plasmonic modes. We perform exhaustive characterization that includes vibrating sample magnetometry (VSM), ellipsometry, optical transmission spectroscopy, and electron energy loss spectroscopy (EELS) to better understand the interplay between composition, physical and chemical morphology, and magnetic and optical properties.

MATERIAL SYNTHESIS AND INITIAL CHARACTERIZATION

Sputtered Thin Film. Initial chemical and structural characterization of the Au_xCo_{1-x} thin-film system was conducted on a 400 nm thick film deposited on a 100 mm SiO2-coated Si substrate. The thin film was achieved via simultaneous sputtering of elemental Au and Co targets (Figure S1), resulting in a compositional gradient across the substrate. The surface topology, chemical segregation, and crystal structure of five compositions (ranging from Au₁₄Co₈₆ to Au₈₇Co₁₃) were characterized via scanning electron microscopy (SEM), energy-dispersive X-ray spectroscopy (EDX), and X-ray diffraction (XRD), with results included in Figure S1. The as-deposited thin films exhibited an extremely fine nanogranular FCC solid solution evidenced by the linear shift in lattice parameter consistent with the variation in chemical composition. Annealing at both 350 and 520 °C for 2 h resulted in a significant increase in grain size and clear evidence of phase separation in SEM and EDX. At both temperatures, Au and Co are immiscible; however, at 350 °C, Co would be expected to form an HCP crystal structure, whereas at 520 °C, FCC is the equilibrium crystal structure. The XRD results after annealing clearly exhibit the phase-

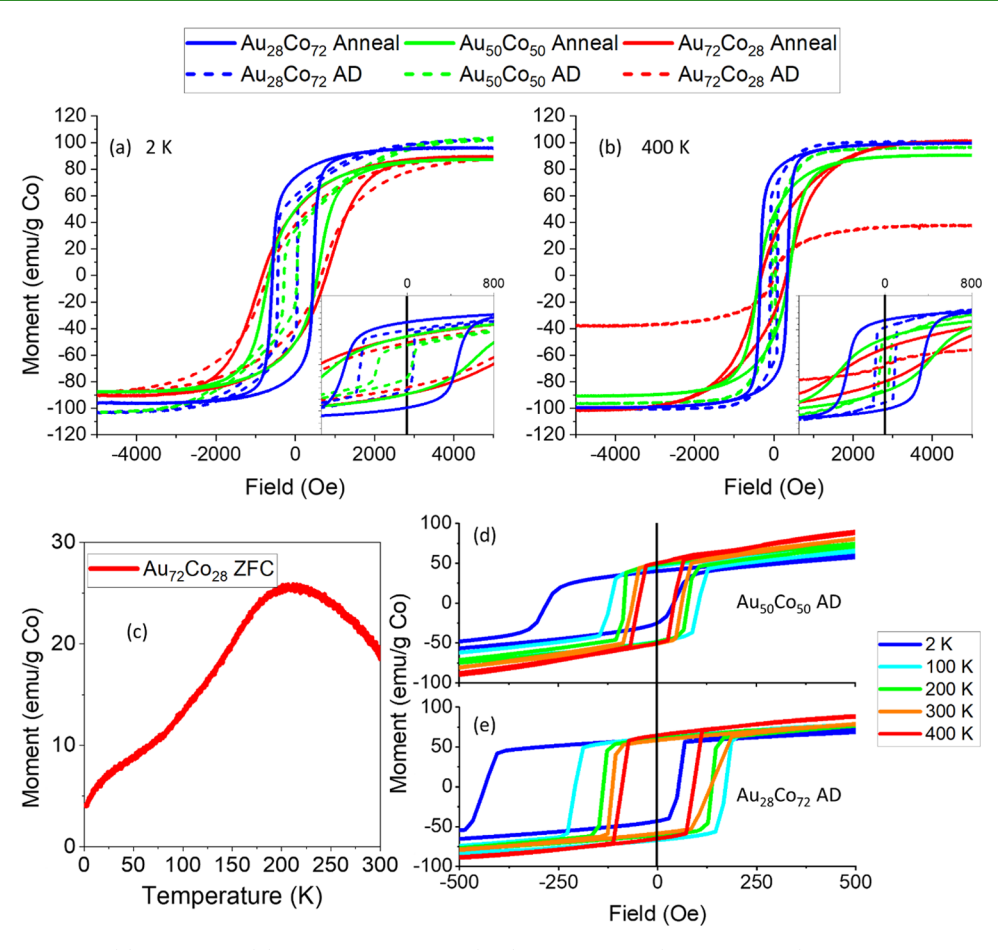


Figure 2. M vs H plots at 2 K (a) and 400 K (b) for the as-deposited (AD) and annealed (450 °C for 2 h) $Au_{72}Co_{28}$, $Au_{50}Co_{50}$, and $Au_{72}Co_{28}$ thin films, (c) ZFC plot for the as-deposited Au-rich thin film, and (d, e) temperature dependence of the $Au_{50}Co_{50}$ and $Au_{72}Co_{28}$ samples.

separated Au FCC peaks, but the lack of the Co signal makes differentiating between the HCP and FCC Co impossible. Thus, all subsequent heat treatments are in the high-temperature FCC+FCC portion of the phase diagram, and the lower-temperature HCP region is not considered. Following initial characterization, three compositions, $Au_{28}Co_{72}$, $Au_{50}Co_{50}$, and $Au_{72}Co_{28}$, were sputtered at a thickness of approximately 60 nm for magnetic and optical measurements. SEM and EDX characterization of these thin films can be found in the Supporting Information (Figure S2).

Nanoparticles via Pulsed Laser-Induced Dewetting (PLiD). Au_xCo_{1-x} spherical cap nanoparticles, as seen in Figure 1, were synthesized from 10 nm thin films via PLiD. While nanoparticles fabricated for magnetic testing were laser treated on 500 μ m thick Si substrates (coated with 100 nm SiO₂), optical measurements necessitated electron and optically transparent substrates. A 40 nm thick low-stress SiN_x membrane ($\approx 150 \ \mu \text{m} \times \approx 150 \ \mu \text{m}$) supported by a 300 μm thick Si frame was used. The previous work³⁵ on 10 nm thick Ag₆₀Ni₄₀ thin films provides approximate heating conditions required to generate nanoparticles on both substrates and suggests a liquid lifetime of approximately 20 ns for dewetting. Finite element thermal simulations shown in Figure 1j indicate that a fluence of ≈140 mJ/cm² provides a sufficient liquid lifetime for the SiO₂-coated Si bulk substrates, while only \approx 40 mJ/cm² is necessary for the thin transparent substrates. Not only are energy input requirements different, the liquid lifetime and cooling times are significantly longer on the thin

membrane compared to a thick substrate (nanoseconds compared to milliseconds).

Figure 1 demonstrates that following PLiD, the nanoparticles appear chemically homogeneous, with no apparent zcontrast, whereas annealing results in distinct contrast indicating phase separation: the dark areas correspond to Co. Post fabrication annealing of bimetallic nanoparticles has been demonstrated as a viable technique to manipulate the nanoparticle chemical morphology in immiscible systems.³⁶ The three different compositions Au₆₆Co₃₄, Au₄₈Co₅₂, and Au₂₂Co₇₈ exhibit similar behaviors following PLiD. Annealing for 20 min, compared to 60 min does not result in markedly different morphology, though there is some coarsening of the phase-separated areas. The Au₆₆Co₃₄ sample is predominantly small Co cores that transition to the surface; a similar behavior is observed in Au₄₈Co₅₂, albeit with larger Co regions, and Au₂₂Co₇₈ is largely Co with Au areas distributed throughout the nanoparticle. There were no observed consistent variations in the nanoparticle chemical morphology associated with changes in the size of the nanoparticles for any composition. XRD measurements of a PLiD sample prior to and after annealing (Figure 1k) indicate that the as-PLiD nanoparticles have a Au_xCo_{1-x} solid-solution structure. Further, the phase separation is confirmed in the 20 min annealed particles via a similar behavior as observed in the annealed thin films. The combination of liquid miscibility, rapid cooling, and slow kinetics allow for the generation of nonequilibrium Au_xCo_{1-x} solid-solution nanoparticles using PLiD. It should be noted

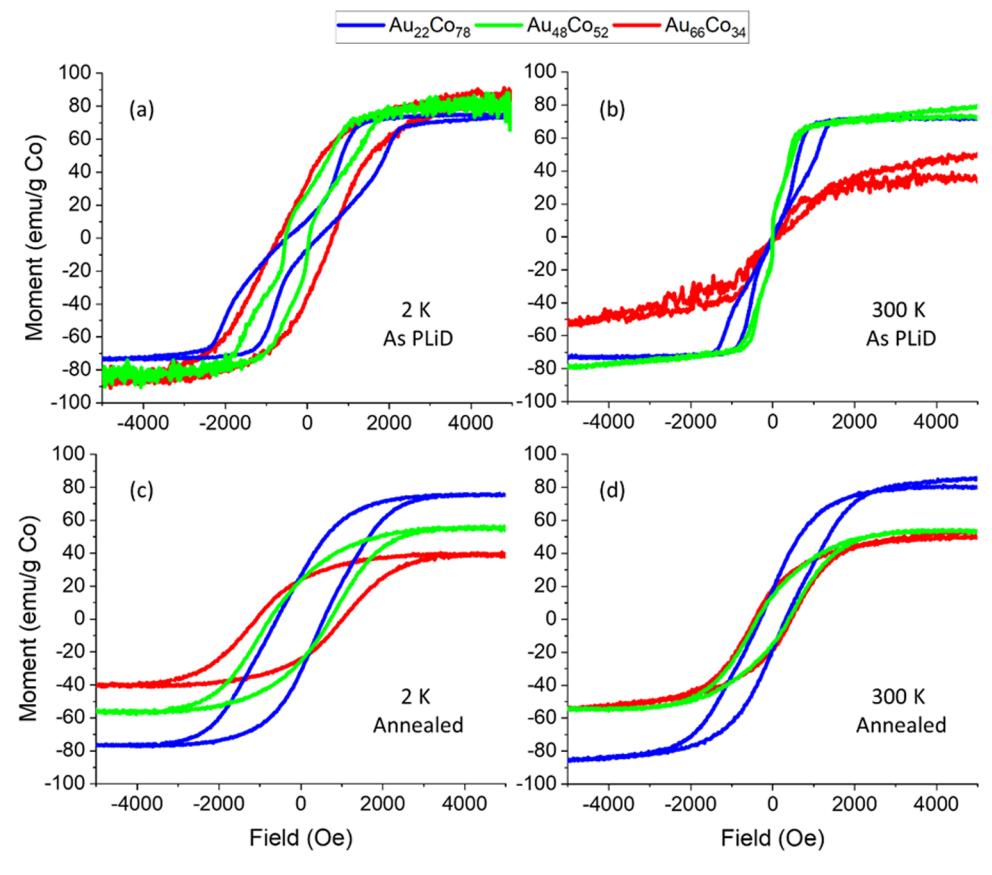


Figure 3. M vs H plots of as-PLiD (a,b) and annealed for 20 min at 580 °C (c, d) nanoparticles with compositions of $Au_{66}Co_{34}$, $Au_{48}Co_{52}$, and $Au_{22}Co_{78}$ at 2 and 300 K.

that the XRD signal is significantly reduced in Figure 1 compared to Figure S1 due to reduced spot size ($\approx 1~\rm cm^2$) and thinner (10 vs 400 nm) deposited thin films. To support the XRD results and demonstrate the nanoparticle solid solution and subsequent phase separation upon annealing, see Figure S3 in the SI for EDX maps of as-PLiD and nanoparticles after annealing. Furthermore, as will be shown below, EELS mapping is suggestive of a homogeneous optical response in the as-PLiD nanoparticles, relative to the phase-separated nanoparticles after annealing.

MAGNETIC PROPERTIES

Thin Films. The magnetic properties of Au_xCo_{1-x} thin films prior to and after annealing were characterized by vibrating sample magnetometry (VSM). The M vs. H plots at two different test temperatures (2 and 400 K) are shown in Figure 2a,b, respectively. At 2 K, all samples exhibit ferromagnetism, as identified by the characteristic coercivity (opening of the hysteresis loop). At 400 K, the coercivity is decreased; however, all of the films remain ferromagnetic, with the exception of the as-deposited Au₇₂Co₂₈ sample. Zero-field cooled magnetization versus temperature measurements of the Au₇₂Co₂₈ sample is included in Figure 2c, showing a global maximum at \approx 210 K, which is commensurate with a closing of the hysteresis loops, indicating superparamagnetic behavior. The magnetic anisotropy of pure Co in the HCP structure is exceptionally high, making the formation of superparamagnetism challenging. Here, the combination of the FCC structure, which is expected to have a much lower magnetic anisotropy, the small grain size (\approx 10 nm), and the prevalence of Au within

the solid solution make this behavior possible. Similar superparamagnetic behavior has been observed in alloyed Au—Co nanoparticles. After annealing, large Co grains form, increasing the blocking temperature to above 400 K and leading to the observed ferromagnetic behavior as seen in Figure 2b. The other as-deposited films exhibit a similar nanogranular structure but do not have this same superparamagnetic behavior. This is due to the reduction of Au in the solid solution, leading to stronger exchange coupling from the larger number of magnetic nearest neighbors, increasing the blocking temperature.

In Figure 2, all magnetic moment measurements have been normalized to the estimated Co mass of each sample. This normalization leads to similar saturation magnetizations for each sample, outside of the Au₇₂Co₂₈ as-deposited film above its blocking temperature. The similarity between the saturation magnetization indicates that Au is not polarized by the adjacent Co atoms and does not contribute significantly to the overall magnetic signal. However, variations in the shape of the magnetic hysteresis loops suggest that there are differences in the reversal behavior that can be linked to the nanostructure of the films. Specifically, in the as-deposited Au₇₂Co₂₈ films, the Co atoms each have, on average, two nearest neighbors Co atoms and four nonmagnetic Au atoms. At low temperatures, small clusters of Co may possess sufficient coupling to achieve stable ferromagnetic ordering; however, these regions are not magnetically connected or are weakly connected. As a result of this weak coupling, the demagnetizing magnetostatic energy, which exists in a three-dimensional (3D) matrix of randomly assembled magnetic elements, causes reversal even in positive

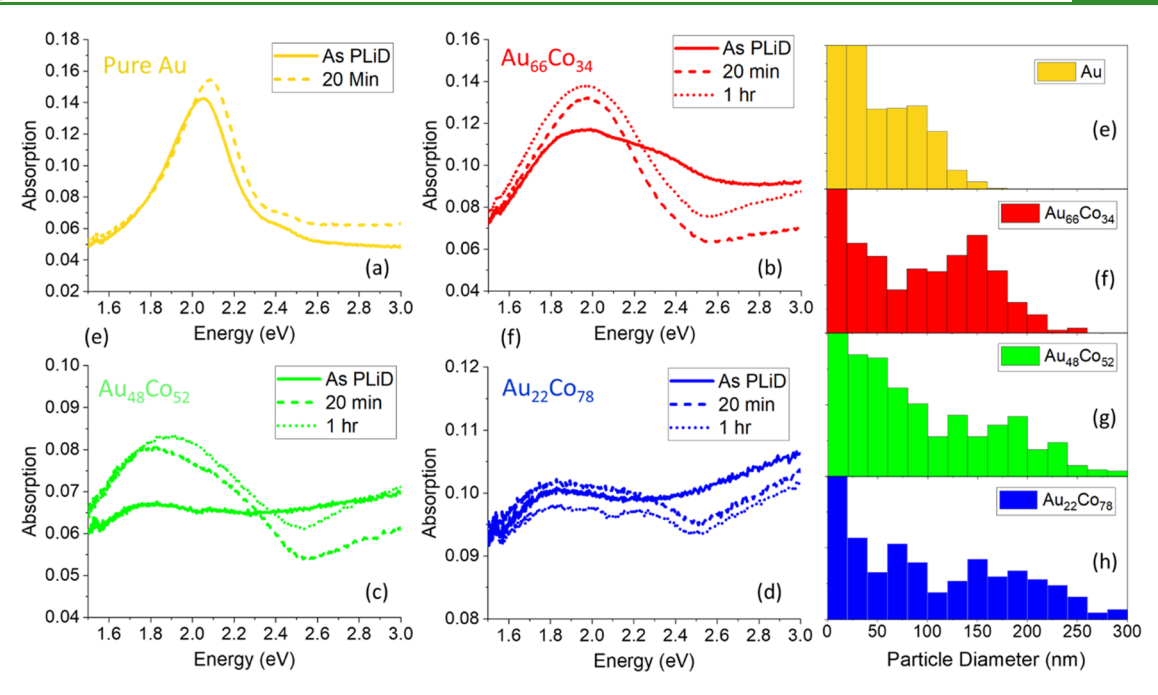


Figure 4. Optical transmission spectra for pure Au (a), $Au_{66}Co_{34}$ (b), $Au_{48}Co_{52}$ (c), and $Au_{22}Co_{78}$ (d) nanoparticle arrays (size distribution included in (e-h)) as-PLiD and following annealing at 580 °C for 20 and 60 min.

fields. Furthermore, with the magnetic clusters effectively isolated, domains are unable to propagate, causing each region to necessarily facilitate its own reversal, manifesting a larger magnetic coercivity. After annealing, phase separation is achieved; however, these new clusters are still far below the single-domain size and remain isolated. For these reasons, the magnetic behavior changes very little—each cluster must still facilitate its own reversal event.

In the other samples ($Au_{50}Co_{50}$ and $Au_{28}Co_{72}$), the magnetic fraction increases, resulting in improved magnetic coupling between the clusters. This improved coupling stabilizes the magnetic network against the demagnetizing effects of the magnetostatic interactions and allows domain walls to propagate through the system. With this change in reversal behavior, defect-mediated domain nucleation causes premature reversal, compared to the single-domain samples, which then propagate rapidly through the network. Additionally, the increased connectivity of the network significantly reduces the pinning site density for the domains. These effects result in a reduced magnetic coercivity, as observed.

Notably, there is a shift in the hysteresis loops of the asdeposited Au₂₈Co₇₂ and Au₅₀Co₅₀ samples toward the negative field. This behavior is attributed to exchange bias³⁷ and implies a coupling between antiferromagnetic and ferromagnetic phases. In these systems, uncompensated spins on the surface of the antiferromagnet are pinned in a fixed orientation by the antiferromagnetic phase but are also exchange coupled to the ferromagnet. This coupling results in an effective field at the interface, biasing the ferromagnet toward alignment with this uncompensated spin, manifesting as a field shift in the hysteresis loop and enhanced magnetic coercivity.³⁷ Indeed, Figure 2d,e shows both of these features for the 2 K measurements. The ferromagnetic component in the material is clearly Co; however, the antiferromagnetic contribution could be attributed to CoO, Co₃O₄, or the interactions between Au and Co. The exchange bias is observed to disappear at T > 100 K and also does not exist in the annealed

films. The Neel temperature of CoO is 293 K, so it is unlikely that the exchange bias is due to CoO. $\rm Co_3O_4$, on the other hand, has a Neel temperature of approximately 30 K; however, the formation of $\rm Co_3O_4$ is observed at elevated temperatures, which should not occur in the as-deposited films. Furthermore, the reduction in exchange bias after annealing does not support the presence of Co oxides because annealing would be expected to increase oxide formation and thus enhance exchange bias. Finally, no peaks for an ordered oxide were identified in the X-ray diffraction patterns. Annealing does, however, reduce the solid solution $\rm Au_x Co_{1-x}$ and with that many of the Au and Co interactions. For these reasons, it appears likely that the exchange bias is primarily due to Au and Co interactions.

Nanoparticles. The magnetic properties of the nanoparticles shown in Figure 1 were also measured using VSM. The as-prepared Au₂₂Co₇₈ and Au₄₈Co₅₂ PLiD nanoparticles, shown in Figure 3a,b, exhibit an open "wasp-waisted" hysteresis loop, suggesting an initial nucleation event with decreasing field, then quasireversible field response through remanence. Based on the nanoparticle size (70-150 nm), there is expected to be both vortex-state and single-domain magnetic configurations, contributing collectively in the bulk measurement to establish the open wasp-wasted loops. 39,40 The combination of both features indicates that the particle size distribution in the solid-solution nanoparticles straddles the vortex-to-single domain boundary, which is determined by the balance between the magnetostatic energy and the exchange. This behavior is prevalent in all as-laser treated nanoparticles at RT and disappears in the Au-rich sample at 2 K. The absence of the wasp-wasted shape in this sample suggests that the nanoparticles have resolved to a singledomain configuration, indicating that the magnetostatic energy is insufficient to overcome the exchange energy. Since the magnetostatic energy increases with decreasing temperature, this suggests that the exchange energy is also increasing with cooling. The wasp-wasted shape disappears in all of the

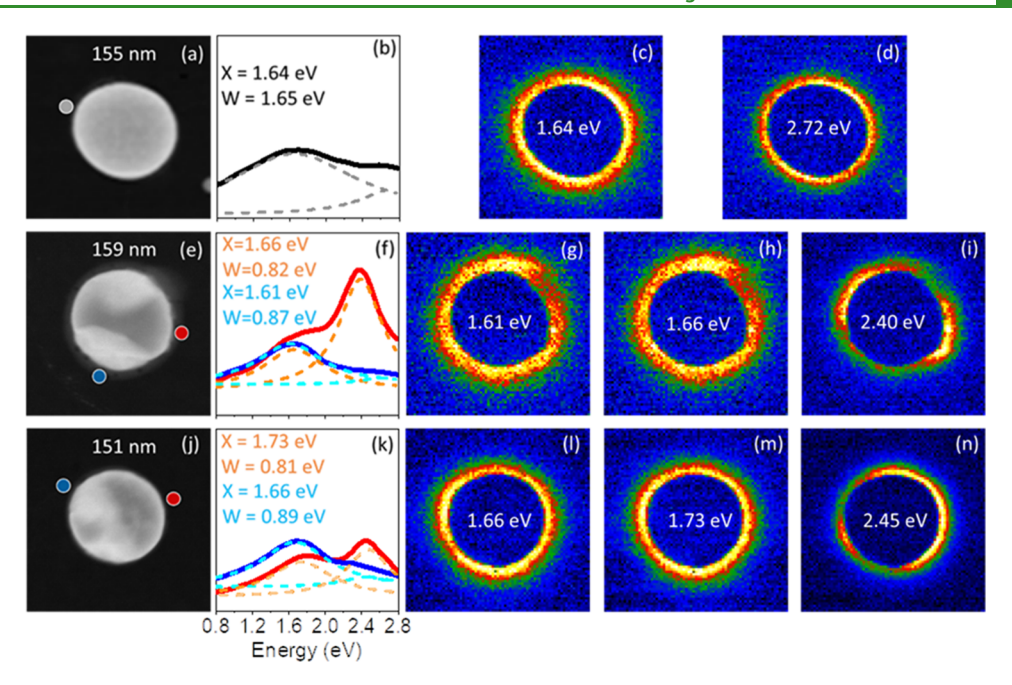


Figure 5. (a, e, and j) HAADF STEM images of three Au_xCo_{1-x} nanoparticles, (b, f, and k) point spectra at the positions indicated in (a, e, and j), and (c, d, g-I, and l-n) spectrum images filtered to the energies indicated.

samples following 20 min of annealing at 580 °C. This can be attributed to the increased exchange energy and smaller magnetic volumes in the phase-separated samples. Specifically, the as-PLiD nanoparticles are relatively homogeneous throughout each individual nanoparticle, possessing both a weak exchange interaction due to the diluted density of magnetic elements and a large magnetic volume—effectively the entire particle. In the annealed nanoparticles, Co precipitates are very small, and each cobalt atom has a much higher density of average magnetic neighbors. Both of these factors favor the single-domain configuration.⁴⁰

Thin-Film Ellipsometry. The optical properties of the as-

OPTICAL PROPERTIES

and near-infrared frequencies.

deposited and annealed (450 °C for 2 h) Au₇₂Co₂₈, Au₅₀Co₅₀, and Au₂₈Co₇₂ thin films were measured via ellipsometry. These results, as well as reference data for Au⁴¹ and Co,⁴² are included in Figure S4 in the SI as a function of photon energy. A simple relationship $\left(-\frac{\varepsilon_1}{\varepsilon_2}\right)$, termed the localized surface plasmon resonance (LSPR) quality factor (Q_{LSPR}), can be used to express the viability of a material for plasmonic applications: this value is plotted in Figure S4a. Below the energy of the Au interband transition (\approx 2.4 eV), the addition of Co, which has a very low-quality factor, greatly reduces Q_{LSPR} compared to pure Au. This behavior is observed in both the as-deposited and annealed films and scales with the amount of Co. Similar damping of the optical properties has been observed in alloyed AuCo nanoparticles fabricated via laser ablation.²⁶ There is, however, clear evidence that phase separation induced through annealing results in a significant (4x) increase in Q_{LSPR} compared to the as-deposited films. Specifically, the annealed Au₇₂Co₂₈ composition suggests that small quantities of phaseseparated Co can be introduced into an Au matrix while maintaining strong optical properties ($Q_{LSPR} = 4$) in the visible

PLiD Nanoparticles. Transmission Spectroscopy. The bulk plasmonic properties of Au_xCo_{1-x} nanoparticle arrays were measured via optical transmission spectroscopy. Figure 4 illustrates the results for pure Au, $Au_{66}Co_{34}$, $Au_{48}Co_{52}$, and $Au_{22}Co_{78}$ nanoparticles prior to and after annealing, along with nanoparticle size distributions for each composition. Whereas the nanoparticle distributions following PLiD for the VSM samples on SiO_2 -coated Si were very consistent, PLiD on SiN_x membranes resulted in variation between the different compositions. Specifically, the $Au_{48}Co_{52}$ and $Au_{22}Co_{78}$ samples have a wider distribution and a larger average diameter compared to the pure Au and $Au_{66}Co_{33}$. An increase in nanoparticle size results in a red-shift in LSPR modes, while a wider distribution leads to a broadening in the collective behavior.

The pure Au PLiD nanoparticles (Figure 4a) produce a sharp peak in absorption at 2.1 eV. This peak can be identified as the LSPR dipole due to the predominance of nanoparticles in the 50–120 nm range.⁴³ Annealing results in a slight increase in peak intensity and blue shift of peak positions, likely due to recrystallization and grain growth of the nanoparticles and perhaps some interdiffusion into the substrate, which slightly decreases the nanoparticle size. None of the as-PLiD Au_xCo_{1-x} samples exhibit a comparable absorption peak, with only the Au₆₆Co₃₄ nanoparticles yielding a definitive, though broad, peak in the same energy range. The intensity of the absorption peak associated with the LSPR dipole mode in all three samples is enhanced by annealing for 20 min at 580 °C (most pronounced in Au₆₆Co₃₄ and Au₄₈Co₅₂) and then improved slightly beyond that with an additional 40 min of annealing. As demonstrated, the annealing results in phase separation, where the phase-separated nanoparticles exhibit a stronger plasmon resonance relative to the solid solution. After annealing, the transmission results show that there is a decrease in the absorption peak height with increasing Co. Thus, despite the variation in nanoparticle size distributions, the transmission spectroscopy results are consistent with the ellipsometry thin-film results, namely, the optical performance

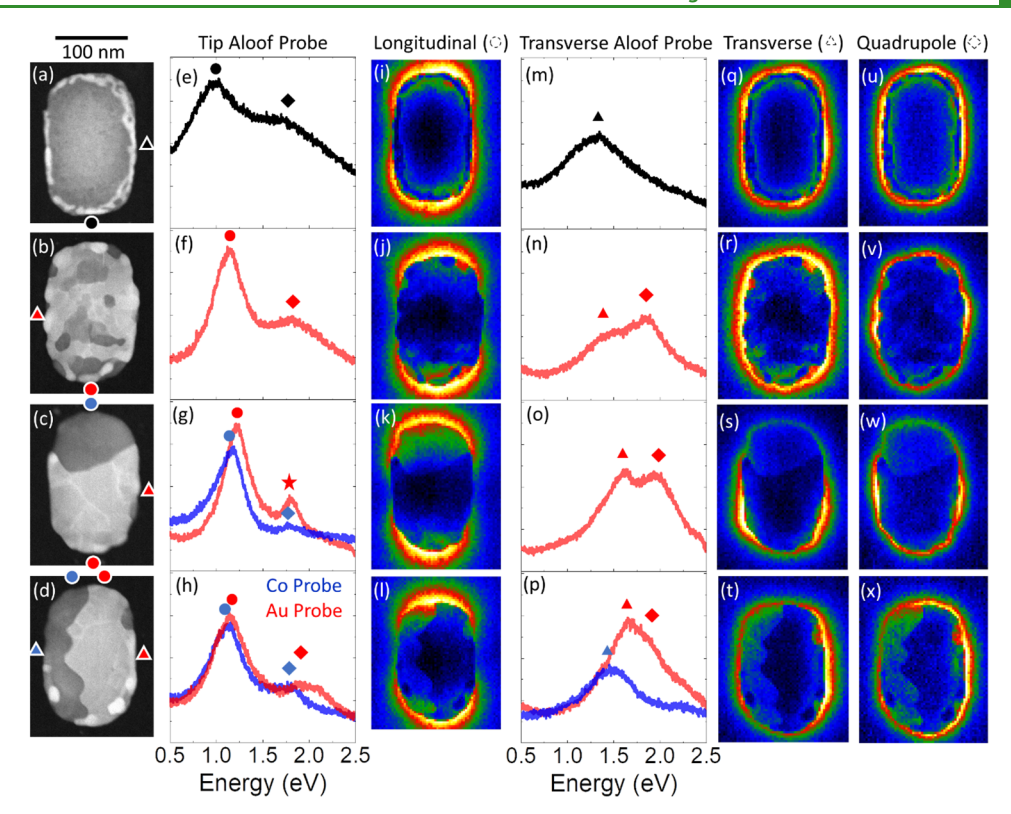


Figure 6. (a-d) HAADF images of four Au_xCo_{1-x} rods with different chemical morphologies: (a) solid solution, (b) interspersed Co grains in a Au matrix, (c) longitudinal Janus, and (d) transverse Janus, (e-h) point spectra from a tip position (circle in a-d), where the color signifies the chemical probed: Au (red), Co (blue), and solid solution (black). The spectrum images filtered to the energy of the dipole mode (circle in e-h) are included in (i)-(l). Point spectra for an aloof position halfway along the longitudinal length (triangle in a-d) are shown in (m)-(p), and spectrum images of the transverse dipole (triangle) are included in (q)-(t), while the longitudinal quadrupole (diamond) is shown in (u)-(x).

scales with Co composition and the $\operatorname{Au}_x\operatorname{Co}_{1-x}$ optical properties are significantly improved via phase separation induced through annealing.

Electron Energy Loss Spectroscopy. Electron energy loss spectroscopy (EELS) provides a tool to measure individual nanoparticles and thus directly observe the effect of chemical morphology on optical properties. In Figure 5, three spherical cap nanoparticles with different chemical morphologies, but very similar composition (Au₅₆Co₄₄) and size (155 nm), are analyzed via EEL point spectra at selected positions of interest as well as spectrum images. The point spectra shown in Figure 5 were fitted to two Lorentzian functions corresponding to the LSPR dipole mode and the quasiplanar mode, which is the high-energy LSPR limit that is nearly degenerate with the surface plasmon polariton energy. The positions of these fits were used to generate the energy filtering criteria in the spectrum images. The first nanoparticle (Figure 5a) was dewetted via PLiD with no further heat treatment (directly comparable to the as-PLiD plots in Figure 4). Here, there is one broad dipole peak at 1.64 eV, shown in Figure 5b. The spectrum image filtered to this energy, Figure 5c, shows that this peak is uniformly distributed around the nanoparticle. The second, and much smaller, peak is associated with the quasiplanar mode; it should be noted that this peak is blueshifted compared to the expected pure Au quasiplanar mode, which is consistent with observations in alloyed Au-Fe nanoparticles.44

Nanoparticles in Figure 5e—i and j—n were laser treated and then annealed at 450 °C for 2 h to prompt phase separation. As observed in Figure 1, there is a wide range of nanoparticle

morphologies following annealing, and here two different morphologies have been selected. Note that the contrast between the two phases is the inverse of Figure 1, i.e., in Figure 5 the darker contrast corresponds to Au due to the highannular angle dark-field (HAADF) transmission mode. Blue is used to indicate Co and red for Au in Figure 5e,f and j,k. Beyond the added evidence that phase separation enhances plasmonic performance (demonstrated here by the reduction of FWHM and emergence of the quasiplanar peak in f and k compared to b), the high spatial resolution of EELS reveals that the phase-separated nanoparticles contain distinct site specific behavior. This results in three important findings: (1) despite the large discrepancy in quality factor between Au and Co, the LSPR dipole peak is not damped at Co aloof positions compared to Au aloof positions, (2) there is a small red-shift in the resonance energy of the LSPR dipole mode at Co aloof positions, and (3) Au aloof positions exhibit high-intensity excitations beyond the LSPR dipole mode, namely, the quasiplanar peak at 2.4 eV, whereas only a small high-energy shoulder is observed from Co aloof positions.

Expanding on these observations is not feasible with spherical cap nanoparticles, as the inherent symmetry makes distinguishing LSPR modes challenging. Thus, electron beam lithography and annealing were leveraged to fabricate solid solution and phase-separated nanorods with an aspect ratio of 1.5 to better elucidate the nanoscale influence of chemical morphology on the plasmonic properties of Au_xCo_{1-x}. Figure 6 includes point spectra and spectrum images of Au₅CO₄₄ rods with the following morphologies: solid solution (a), interspersed Co grains in Au matrix (b), longitudinal Janus

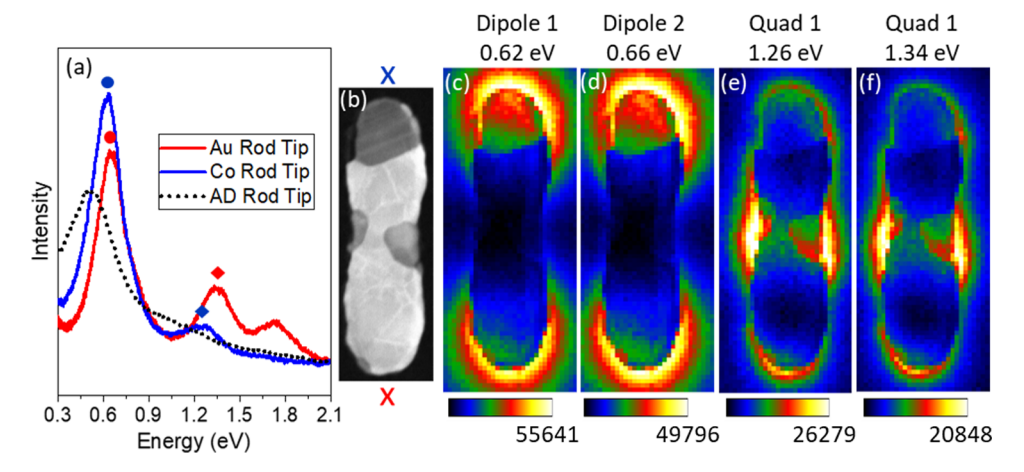


Figure 7. (a) Point spectra collected at the two ends of the phase-separated rod shown in (b) with the blue indicating a Co position and the red indicating a Au position; the dotted black line is a spectrum from an as-deposited solid-solution rod of the same length; (c-f) spectrum images filtered to the energies of the first and second dipole resonances (c, d) and the first and second quadrupole energies (e, f). The circles are used to denote the longitudinal dipole mode, and the diamonds indicate the quadrupole mode.

(c), and transverse Janus (d). These rods exhibit three primary peaks attributed to the longitudinal dipole and quadrupole, as well as transverse dipole LSPR modes. Plots in Figure 6e-h show EELS point spectra taken at rod tip positions (positions shown by circles in Figure 6 HAADF images), where excitation of the longitudinal dipole mode is at a maximum, and the longitudinal quadrupole can be observed as a secondary peak. Spectrum images in Figure 6i-l are filtered to the energy of the dipole peak, which is indicated via a circle in the spectra in Figure 6e-h. Point spectra included in m-p were taken at a position halfway along the longitudinal length (triangle in Figure 6), where the transverse dipole and longitudinal quadrupole modes can be excited. Spectrum images in q-t and u-x are filtered to the energy of the transverse dipole and quadrupole mode, respectively. A diamond (transverse dipole) and triangle (longitudinal quadrupole) are used to indicate the energy selected for the spectrum images. The appropriate energy for each spectrum image was determined via Lorentzian peak fitting, and the fitted peak positions for each rod are included in Table S2. As with Figure 5, red is used to indicate a Au probe position, blue a Co position, and black a solidsolution position.

Regardless of the distribution of phase-separated precipitates in nanorods, there is a similar enhancement, and blue shift, in the LSPR dipole mode compared to the solid solution state. This observation in the speckled rod in Figure 6b indicates that small, isolated phase separation is sufficient to provide enhancement of the dipole mode. The asymmetry between Au and Co probe positions in the dipole mode is greatest in the longitudinal Janus configuration (c) in which the plasma oscillation is perpendicular to the phase-separation interface. In this rod, the Co probe position yields a slight reduction in EELS intensity as well as the greatest red-shift among the chemical morphologies. The transverse Janus rod, in which the longitudinal dipole is parallel to the phase-separation interface, exhibits nearly identical dipole excitation from the Au or Co aloof positions. This can, at least in part, be attributed to the very close proximity of the probe positions in the parallel configuration leading to some mixture in the response.

Consistent with Figure 5, the LSPR modes beyond the longitudinal dipole (transverse dipole and longitudinal quadrupole) are severely damped at Co aloof positions. This is most

noticeable in the longitudinal Janus morphology spectrum images (s and w), which exhibit much greater intensity around the Au portion of the rod than the Co. It is also apparent in the point spectra (g), where a Co tip probe position excites only a single secondary peak that is barely above the noise level. In the tip positions of the transverse Janus configuration (d), the differences are less pronounced. Specifically, both the Au and Co tip point spectra in (h) exhibit a similar intensity quadrupole peak. The quadrupole spectrum image (x) shows that the decay in intensity along the top tip position (where the point spectra were taken) is not abrupt at the Au/Co interface and instead extends into the Co portion of the rod. Thus, it appears that the similarity in the quadrupole signal at the Au and Co tip positions is due to the close proximity of the aloof positions. Conversely, the transverse position spectra (p), where the Au and Co aloof positions are more isolated from each other, exhibit a significant reduction in the transverse dipole mode at a Co position compared to the Au, and no apparent longitudinal quadrupole peak, though it is potentially convolved within the reduced transverse peak.

It should be noted that in the longitudinal Janus rod, the secondary peak at the Au tip position in Figure 6g, denoted as a star, is red-shifted from the fitted value determined via (o) and shown in (w). This shift could be attributed to challenges in fitting the spectra in (o), variations in the peak energy based on the probe position, or the emergence of a separate mode caused by the truncated Au portion of the rod.

As the structures in Figures 5 and 6 have relatively high resonance energy modes, it remains unclear if the damping beyond the longitudinal dipole in the Co is associated with an energy limitation, potentially from the Co interband transitions, or due to reduced excitation efficiency in more complicated polarization states. Figure 7 shows the red shifted point spectra, a HAADF image, and spectrum images of a significantly longer (410 nm) phase-separated Au₆₈Co₃₂ rod that is primarily Au, with Co located on the right end as well as at the center of the rod. Note the black dotted spectrum is from a similar as-deposited solid-solution rod for comparison.

The point spectra (a) and spectrum images (c, d) at the two rod ends indicate that the intensity of the longitudinal dipole mode remains undamped, and in this case is stronger, at the Co tip position compared to the Au. Despite the reduction of LSPR energies, the higher-order modes continue to demonstrate a much greater intensity when excited at the Au tip compared to the Co tip. The Co probe position results in a weak quadrupole excitation that is again red-shifted. Beyond this, the 1.7 eV hexapole mode observed at the Au end has zero intensity at the cobalt end. Figure 7e,f shows spectrum images filtered to the higher-energy quadrupole modes determined from the Co (e) and Au (f) point spectra. Both possess the expected behavior of a quadrupole polarization; however, the central node is noticeably shifted toward the Au end in each case. This trend combined with the reduced quadrupole signal at the Co probe position provides further evidence that higher-order and higher-energy modes do not propagate through the Co end efficiently. Interestingly, the Co precipitates located at the quadrupole antinode center position do not appear to be damped in the spectrum images. This is likely another instance where the close proximity of Au results in propagation into Co.

Combining the results from Figures 5-7, the longitudinal dipole mode is undamped at Co aloof positions compared to Au at energies of 0.6, 1, and 1.6 eV, whereas higher-order modes exhibit a consistent reduction in the signal at Co aloof positions regardless of energy (>1.25 eV). The only instances where a significant reduction in the intensity of these higherorder modes is not exhibited is when the probed Co position is in close proximately to a large Au region. While it is possible that Co interband transitions are contributing to the damping of the higher-order modes, the lack of a clear energy cutoff combined with markedly differing behaviors between the modes at similar energies indicates that there is another source of the damping. Although the mechanism is not clear, the plasmon polarization state appears to create a large discrepancy in the efficiency of LSPR propagation in phase-separated Au_rCo_{1-r} nanostructures.

As demonstrated in these rods, interesting LSPRs emerge depending on the phase separation length scale and orientation. Thus, harnessing the free-energy landscape in metastable solid solutions to equilibrium phase-separated plasmonic and magneto-plasmonic architectures can be explored as new routes to optical and magneto-optical materials.

CONCLUSIONS

Solid solution and phase-separated Au_xCo_{1-x} thin films and nanoparticles were fabricated via a combination of cosputtering, PLiD, and annealing. The optical and magnetic properties were found to be strongly dependent on this variation in chemical morphology. Altering the chemical composition presented further opportunity to tune the material properties. The addition of sufficient Au (72 atom %) into the Au_xCo_{1-x} solid solution thin film resulted in superparamagnetic behavior, despite the high magnetic anisotropy of Co, while nanoparticles with > 50 atom % Co exhibited a wasp-waisted hysteresis due to magnetic vortex generation (not observed with 66 atom % Au). Traditional ferromagnetic behavior was then achieved in both the thin films and nanoparticles after the formation of phase-separated Au and Co grains. Annealing also removed low-temperature exchange bias that was observed in the as-deposited and as-PLiD samples, which suggests that the Au-Co solid-solution interactions were causing this behavior. The optical properties of Au_xCo_{1-x} were severely damped in the as-deposited solid-solution state in both thin films and isolated nanostructures, as evidenced by ellipsometry, optical

transmission, and EELS. This behavior was exacerbated by increasing the Co composition. Significant enhancement of the optical properties was observed for both the thin films and nanoparticles in the phase-separated samples. EELS analysis of individual nanostructures demonstrated that the longitudinal dipole LSPR peak was mostly independent of the configuration of the phase-separated precipitates and exhibited a similar intensity when probing from a Co or Au position. Beyond the longitudinal dipole, however, there was a consistent trend of reduced intensity in the higher-order modes associated with a Co probe position. Thus, we have demonstrated via synthesis techniques promoting nonequilibrium solid solutions and thermal annealing that the magnetic and optical properties in immiscible material systems can be altered through chemical composition and morphology. This magneto-plasmonic bifunctionality, and insights into the tunability of these properties, could have promise in applications such as cancer treatment and/or detection.

METHODS

Radio Frequency Magnetron Sputtering and Annealing. Two pure (Au and Co) sputtering targets were sputtered simultaneously with the substrate rotating (no compositional gradient) and with the substrate stationary (chemical gradient from one target to the other) depending on experimental requirements. A base pressure of less than 3×10^{-7} Torr, sputtering pressure of 5×10^{-7} 10⁻³ Torr, and Ar flow of 25 sccm were used for all samples. For combinatorial (no rotation) samples, a bias of 20 W for Au and 200 W for Co resulted in a center composition of Au₅₀Co₅₀. These conditions resulted in a deposition rate of 2 nm/min, measured via profilometry. Specific sputtering conditions for the remaining samples are included in Table S1 in the Supporting Information. A substrate of 500 µm thick Si with a coating of 100 nm SiO₂ was used for all samples other than those used for transmission spectroscopy, and EELS. For these measurements, thin 40 nm 150 \times 150 μ m SiN_x membranes supported by a 300 μm thick Si frame were used. Annealing conditions for all prepared samples can be found in the Supporting Information.

Pulsed Laser-Induced Dewetting (PLiD). Pulsed laser dewetting is a process in which a thin film (typically <20 nm thick) is irradiated with a pulsed laser sufficient to heat the film and induce dewetting. One common regime is pulsed laser-induced dewetting in the $\sim 10-20$ ns timescale. ⁵⁻⁸ In this case, the laser irradiance used is sufficiently high to liquefy the film, where the liquid lifetime is on the order of tens of nanoseconds. 45 During the liquid lifetime, thin-film instabilities induce the dewetting of holes which retract and coalesce into a web of rivulets which subsequently break up into nanoparticles due to Rayleigh–Plateau instabilities. 5,6,27,46 A nanoparticle distribution related to the instability time- and length-scale results. While a significant amount of work has been devoted to the dewetting of elemental metal films, recently, the pulsed laser-induced dewetting of miscible 43,47-49 and immiscible metals 34,50-52 has also been studied both experimentally and via molecular dynamics⁵³ modeling and continuum simulations.35

Photothermal heating was conducted using a 248 nm KrF excimer laser. Experiments were conducted in a pulsed mode using a 1/e² Gaussian pulse width of 18 ns and a top hat spatial distribution. The PLiD samples on thick Si (VSM) were heated with five laser pulses with a fluence of 140 mJ/cm². A single pulse with a fluence of 40 mJ/ cm² was used for the samples supported by the SiN_x membrane (optical transmission spectroscopy and EELS).

Scanning Electron Microscopy and Energy-Dispersive X-ray Spectroscopy. Energy-dispersive X-ray spectroscopy (EDX) and scanning electron microscopy (SEM) were conducted on a Carl Zeiss MERLIN SEM. The initial ≈400 nm combinatorially sputtered Au_xCo_{1-x} thin film (as-deposited and annealed) was characterized at five points separated by 20 mm along the composition gradient. For EDX, an accelerating voltage of 20 kV was used. The second

combinatorically sputtered thin film (\approx 60 nm) and the co-sputtered films were characterized with the same parameters. In addition to large area spectra used to determine chemical composition, spatial EDX maps were also collected to observe the nanoscale chemical morphology. Particle size distributions in the PLiD samples and grain size in the thin films were determined with SEM images and the built-in particle analysis plugin in ImageJ.

X-ray Diffraction. X-ray diffraction patterns were measured using a Malvern Panalytical Empyrean diffractometer. A 2θ -omega scan with an omega offset of -4.5° was run with a Cu tube (0.154 nm) with an angle sweep from 30° to 110° . Measurements were taken approximately coincident to where the five EDX scans were performed across both the as-deposited and annealed sample. The $Au_{50}Co_{50}$ as-PLiD and annealed samples were characterized with the same parameters.

Ellipsometry. A JA Woollam M-2000U ellipsometer was used to measure ε_1 and ε_2 as a function of wavelength with a spot size of approximately 1 cm \times 1 mm. The approximate thickness of each sample was 60 nm, which was sufficient to avoid substrate effects. The raw data was fitted using an effective medium approximation (EMA) model in which the composition of each component was estimated using the EDX data. The two metal components were then fitted using a spline model.

Vibrating Sample Magnetometry. A vibrating sample magnetometer (VSM) on a PPMS DynaCool was used to obtain the magnetic properties of $\mathrm{Au_xCo_{1-x^*}}$. The measurement time per point was 2 s. Samples were field cooled in 1000 Oe to 2 K, then hysteresis loops were measured from −5000 to 5000 Oe between 2 and 400 K for the thin-film samples and at 2 and 300 K for the nanoparticle samples. The sample size was ≈4 mm × 4 mm, and the mass normalization was conducted by measuring each sample, subtracting the substrate and then using composition from EDX and thickness from profilometry to determine the Co mass.

Thermal Finite Element Modeling. To approximate the photothermal heating of $\operatorname{Au}_x\operatorname{Co}_{1-x}$ films, a thermal finite element model (FEM) was utilized. Here, a heat source was applied at the $\operatorname{Au}_x\operatorname{Co}_{1-x}$ surface (z=0 nm), in the same manner as.^{4,54} The governing equation for the heat flow is listed below

$$\rho C_p \frac{\mathrm{d}T}{\mathrm{d}t} = \nabla \cdot (k \nabla T) + Q(x, y, z)$$

$$Q(x, y, z) = \frac{2\alpha}{\pi w^2} P(1 - R)G(t) \exp(-\alpha z)$$

The terms α and R indicate the absorption coefficient and the reflectivity, respectively, which were determined from the ellipsometry measurements for different compositions. The value w is the full width of the laser beam at $1/e^2$ of the maximum fluence. The laser fluence is demonstrated as P. G(t) represents the temporal Gaussian of the KrF laser. The edges of the suspended membrane were assigned a boundary condition of room temperature to approximate the thick Si frame. The samples heated on thick Si did not require a boundary condition. The material properties were assumed to be constant, and thermal effects of phase transitions were ignored.

Transmission Spectroscopy. Optical transmission spectroscopy was conducted on the as-deposited and annealed PLiD samples. A 1 mm aperture was for all measurements, and photon energies from 1.5 to 3 eV are included.

Electron Energy Loss Spectroscopy. A Nion aberration-corrected high-energy resolution monochromated EELS—STEM (HERMES) operated at an accelerating voltage of 60 kV was used to obtain the spectra and spectrum images. The convergence and collection semiangles used for the spectrum acquisition were 30 and 15 mrad, respectively. The energy resolution (full width at half-maximum of the zero-loss peak) was approximately 20 meV. The EEL spectra presented were normalized to the zero-loss peak. For the point spectra, an acquisition time of 0.1 s was used, and a total of 50 frames were summed. An acquisition time of 0.1 s was also used for the spectrum images, with an energy filtering range of +/- 0.5 eV used in the figures.

ASSOCIATED CONTENT

Solution Supporting Information

The Supporting Information is available free of charge at https://pubs.acs.org/doi/10.1021/acsami.2c02028.

Additional structural and compositional characterization of $\mathrm{Au}_x\mathrm{Co}_{1-x}$ thin films and nanoparticles, sputtering and annealing parameters, ellipsometry, and tabulated EELS peak positions for Figure 6 (PDF)

AUTHOR INFORMATION

Corresponding Author

Philip D. Rack — Department of Materials Science and Engineering, University of Tennessee, Knoxville, Tennessee 37996, United States; orcid.org/0000-0002-9964-3254; Email: prack@utk.edu

Authors

David A. Garfinkel – Department of Materials Science and Engineering, University of Tennessee, Knoxville, Tennessee 37996, United States; oorcid.org/0000-0002-7593-1868

Nan Tang – Department of Materials Science and Engineering, University of Tennessee, Knoxville, Tennessee 37996, United States

Grace Pakeltis — Department of Materials Science and Engineering, University of Tennessee, Knoxville, Tennessee 37996, United States; orcid.org/0000-0003-1478-4654

Reece Emery – Department of Materials Science and Engineering, University of Tennessee, Knoxville, Tennessee 37996, United States

Ilia N. Ivanov — Center for Nanophase Materials Sciences, Oak Ridge National Laboratory, Oak Ridge, Tennessee 37831, United States; orcid.org/0000-0002-6726-2502

Dustin A. Gilbert – Department of Materials Science and Engineering, University of Tennessee, Knoxville, Tennessee 37996, United States; oorcid.org/0000-0003-3747-3883

Complete contact information is available at: https://pubs.acs.org/10.1021/acsami.2c02028

Notes

The authors declare no competing financial interest.

ACKNOWLEDGMENTS

DAG, RE, GP, and PDR acknowledge support from the National Science Foundation under grant NSF DMR 1709275. Magnetometry results were supported by the U.S. Department of Energy, Office of Science, Office of Basic Research CAREER program under Award Number DE-SC0021344. All of the authors acknowledge that the electron beam lithography, EELS, SEM/EDX, ellipsometry, optical transmission spectroscopy, and nanofabrication were conducted at the Center for Nanophase Materials Sciences, which is a DOE Office of Science User Facility.

REFERENCES

- (1) Collette, R.; Wu, Y.; Olafsson, A.; Camden, J. P.; Rack, P. D. Combinatorial Thin Film Sputtering Au XAl1- x Alloys: Correlating Composition and Structure with Optical Properties. *ACS Comb. Sci.* **2018**, 20, 633–642.
- (2) Boldman, W. L.; Garfinkel, D. A.; Collette, R.; Jorgenson, C. S.; Pradhan, D. K.; Gilbert, D. A.; Rack, P. D. Exploring the Composition, Phase Separation and Structure of AgFe Alloys for Magneto-Optical Applications. *Mater. Sci. Eng., B* **2021**, 266, No. 115044.

- (3) Collette, R.; Wu, Y.; Rack, P. D. Correlating the Optical Property Evolution in the Au-Ni Binary Thin Films: From Metastable Solid Solution to Phase Separated Alloy. *J. Alloys Compd.* **2019**, 793, 695–704.
- (4) Wu, Y.; Liu, C.; Moore, T. M.; Magel, G. A.; Garfinkel, D. A.; Camden, J. P.; Stanford, M. G.; Duscher, G.; Rack, P. D. Exploring Photothermal Pathways via in Situ Laser Heating in the Transmission Electron Microscope: Recrystallization, Grain Growth, Phase Separation, and Dewetting in Ag0.5Ni0.5 Thin Films. *Microsc. Microanal.* 2018, 24, 647–656.
- (5) Diez, J. A.; Kondic, L. On the Breakup of Fluid Films of Finite and Infinite Extent. *Phys. Fluids* **2007**, *19*, No. 072107.
- (6) Diez, J. A.; González, A. G.; Kondic, L. On the Breakup of Fluid Rivulets. *Phys. Fluids* **2009**, *21*, No. 082105.
- (7) Fowlkes, J. D.; Kondic, L.; Diez, J.; Wu, Y.; Rack, P. D. Self-Assembly versus Directed Assembly of Nanoparticles via Pulsed Laser Induced Dewetting of Patterned Metal Films. *Nano Lett.* **2011**, *11*, 2478–2485.
- (8) Rack, P. D.; Guan, Y.; Fowlkes, J. D.; Melechko, A. V.; Simpson, M. L. Pulsed Laser Dewetting of Patterned Thin Metal Films: A Means of Directed Assembly. *Appl. Phys. Lett.* **2008**, 92, No. 223108.
- (9) Amendola, V.; Meneghetti, M. Laser Ablation Synthesis in Solution and Size Manipulation of Noble Metal Nanoparticles. *Phys. Chem. Chem. Phys.* **2009**, *11*, 3805–3821.
- (10) Loza, K.; Heggen, M.; Epple, M. Synthesis, Structure, Properties, and Applications of Bimetallic Nanoparticles of Noble Metals. *Adv. Funct. Mater.* **2020**, *30*, No. 1909260.
- (11) Ealia, S. A. M.; Saravanakumar, M. P. A Review on the Classification, Characterisation, Synthesis of Nanoparticles and Their Application. *IOP Conf. Ser.: Mater. Sci. Eng.* **2017**, 263, No. 032019.
- (12) Sharma, D.; Kanchi, S.; Bisetty, K. Biogenic Synthesis of Nanoparticles: A Review. *Arabian J. Chem.* **2019**, *12*, 3576–3600.
- (13) Espinosa, A.; Bugnet, M.; Radtke, G.; Neveu, S.; Botton, G. A.; Wilhelm, C.; Abou-Hassan, A. Can Magneto-Plasmonic Nanohybrids Efficiently Combine Photothermia with Magnetic Hyperthermia? *Nanoscale* **2015**, *7*, 18872–18877.
- (14) Tomitaka, A.; Arami, H.; Raymond, A.; Yndart, A.; Kaushik, A.; Jayant, R. D.; Takemura, Y.; Cai, Y.; Toborek, M.; Nair, M. Development of Magneto-Plasmonic Nanoparticles for Multimodal Image-Guided Therapy to the Brain. *Nanoscale* **2017**, *9*, 764–773.
- (15) Tomitaka, A.; Arami, H.; Huang, Z.; Raymond, A.; Rodriguez, E.; Cai, Y.; Febo, M.; Takemura, Y.; Nair, M. Hybrid Magneto-Plasmonic Liposomes for Multimodal Image-Guided and Brain-Targeted HIV Treatment. *Nanoscale* **2018**, *10*, 184–194.
- (16) Huang, L.; Ao, L.; Hu, D.; Wei, W.; Sheng, Z.; su, wu. Magneto-Plasmonic Nanocapsules for Multimodal-Imaging and Magnetically Guided Combination Cancer Therapy. *Chem. Mater.* **2016**, *28*, 5896–5904.
- (17) Amendola, V.; Scaramuzza, S.; Litti, L.; Meneghetti, M.; Zuccolotto, G.; Rosato, A.; Nicolato, E.; Marzola, P.; Fracasso, G.; Anselmi, C.; Pinto, M.; Colombatti, M. Magneto-Plasmonic Au-Fe Alloy Nanoparticles Designed for Multimodal SERS-MRI-CT Imaging. *Small* **2014**, *10*, 2476–2486.
- (18) Liu, Y.; Yang, X.; Huang, Z.; Huang, P.; Zhang, Y.; Deng, L.; Wang, Z.; Zhou, Z.; Liu, Y.; Kalish, H.; Khachab, N. M.; Chen, X.; Nie, Z. Magneto-Plasmonic Janus Vesicles for Magnetic Field-Enhanced Photoacoustic and Magnetic Resonance Imaging of Tumors. *Angew. Chem., Int. Ed.* **2016**, 55, 15297–15300.
- (19) Ogut, E.; Menguc, M. P.; Sendur, K. Integrating Magnetic Heads With Plasmonic Nanostructures in Multilayer Configurations. *IEEE Trans. Magn.* **2013**, 49, 3687–3690.
- (20) Li, Z.; Jin, J.; Yang, F.; Song, N.; Yin, Y. Coupling Magnetic and Plasmonic Anisotropy in Hybrid Nanorods for Mechanochromic Responses. *Nat. Commun.* **2020**, *11*, No. 2883.
- (21) Peiris, E.; Sarina, S.; Waclawik, E. R.; Ayoko, G. A.; Han, P.; Jia, J.; Zhu, H.-Y. Plasmonic Switching of the Reaction Pathway: Visible-Light Irradiation Varies the Reactant Concentration at the Solid—Solution Interface of a Gold—Cobalt Catalyst. *Angew. Chem., Int. Ed.* **2019**, 58, 12032—12036.

- (22) Soulé, J.-F.; Miyamura, H.; Kobayashi, S. Selective Lactam Formation from Amino Alcohols Using Polymer-Incarcerated Gold and Gold/Cobalt Nanoparticles as Catalysts under Aerobic Oxidative Conditions. *Asian J. Org. Chem.* **2012**, *1*, 319–321.
- (23) Marbella, L.; Andolina, C.; Smith, A.; Hartmann, M.; Dewar, A.; Johnston, K.; Daly, O.; Millstone, J. Gold-Cobalt Nanoparticle Alloys Exhibiting Tunable Compositions, Near-Infrared Emission, and High T2 Relaxivity. *Adv. Funct. Mater.* **2014**, *24*, 6532–6539.
- (24) Bahmanrokh, G.; Hashim, M.; Soltani, N.; Ismail, I.; Vaziri, P.; Navaseri, M.; Erfani, M.; Kanagesan, S. High Coercivity Sized Controlled Cobalt—Gold Core—Shell Nano-Crystals Prepared by Reverse Microemulsion. *Mater. Res. Bull.* **2013**, *48*, 4039–4047.
- (25) Cheng, G.; Hight Walker, A. Synthesis and Characterization of Cobalt/Gold Bimetallic Nanoparticles. *J. Magn. Magn. Mater.* **2007**, 311, 31–35.
- (26) Guadagnini, A.; Agnoli, S.; Badocco, D.; Pastore, P.; Pilot, R.; Ravelle-Chapuis, R.; van Raap, M. B. F.; Amendola, V. Kinetically Stable Nonequilibrium Gold-Cobalt Alloy Nanoparticles with Magnetic and Plasmonic Properties Obtained by Laser Ablation in Liquid. *ChemPhysChem* **2021**, *22*, 657–664.
- (27) Khenner, M.; Yadavali, S.; Kalyanaraman, R. Formation of Organized Nanostructures from Unstable Bilayers of Thin Metallic Liquids. *Phys. Fluids* **2011**, 23, 122105–122114.
- (28) Peleg, N.; Shtrikman, S.; Gorodetsky, G.; Felner, I. Magnetic Study of Particle Distribution in Granular AuCo. *J. Magn. Magn. Mater.* **1999**, *191*, 349–353.
- (29) Nabika, H.; Mizuhata, M.; Kajinami, A.; Deki, S.; Akamatsu, K. Preparation and Characterization of Au/Co Nano-Alloys. *J. Electroanal. Chem.* **2003**, 559, 99–102.
- (30) Henger, U.; Korn, D. Electrical Resistivity of Thin Films of AuCo Solid Solutions. *J. Phys. F: Met. Phys.* **1981**, *11*, 2575–2584.
- (31) Maurizio, C.; Michieli, N.; Kalinic, B.; Mattarello, V.; Bello, V.; Wilhelm, F.; Ollefs, K.; Mattei, G. Local Structure and X-Ray Magnetic Circular Dichroism of Au in Au-Co Nanoalloys. *Appl. Surf. Sci.* **2018**, 433, 596–601.
- (32) Yang, K.; Kryutyanskiy, V.; Kolmychek, I.; Murzina, T. V.; Lukaszew, R. A. Experimental Correlation between Nonlinear Optical and Magnetotransport Properties Observed in Au-Co Thin Films. *J. Nanomater.* **2016**, *2016*, No. e4786545.
- (33) Chinni, F.; Spizzo, F.; Montoncello, F.; Mattarello, V.; Maurizio, C.; Mattei, G.; Del Bianco, L. Magnetic Hysteresis in Nanocomposite Films Consisting of a Ferromagnetic AuCo Alloy and Ultrafine Co Particles. *Materials* **2017**, *10*, 717.
- (34) Garfinkel, D. A.; Pakeltis, G.; Tang, N.; Ivanov, I. N.; Fowlkes, J. D.; Gilbert, D. A.; Rack, P. D. Optical and Magnetic Properties of Ag–Ni Bimetallic Nanoparticles Assembled via Pulsed Laser-Induced Dewetting. *ACS Omega* **2020**, *5*, 19285–19292.
- (35) Diez, J. A.; González, A. G.; Garfinkel, D. A.; Rack, P. D.; McKeown, J. T.; Kondic, L. Simultaneous Decomposition and Dewetting of Nanoscale Alloys: A Comparison of Experiment and Theory. *Langmuir* **2021**, *37*, 2575–2585.
- (36) Herz, A.; Friák, M.; Rossberg, D.; Hentschel, M.; Theska, F.; Wang, D.; Holec, D.; Šob, M.; Schneeweiss, O.; Schaaf, P. Facet-Controlled Phase Separation in Supersaturated Au-Ni Nanoparticles upon Shape Equilibration. *Appl. Phys. Lett.* **2015**, *107*, No. 073109.
- (37) Nogués, J.; Schuller, I. K. Exchange Bias. J. Magn. Magn. Mater. 1999, 192, 203–232.
- (38) Roth, W. L. The Magnetic Structure of Co3O4. *J. Phys. Chem. Solids* **1964**, 25, 1–10.
- (39) Tobing, L. Y. M.; Tjahjana, L.; Zhang, D. H.; Zhang, Q.; Xiong, Q. Sub-100-Nm Sized Silver Split Ring Resonator Metamaterials with Fundamental Magnetic Resonance in the Middle Visible Spectrum. *Adv. Opt. Mater.* **2014**, *2*, 280–285.
- (40) Dumas, R. K.; Li, C.-P.; Roshchin, I. V.; Schuller, I. K.; Liu, K. Magnetic Fingerprints of Sub-\$100\phantom{\rule{0.3em}-{0ex}}\mathrm{nm}\$ Fe Dots. *Phys. Rev. B* **2007**, *75*, No. 134405.
- (41) Johnson, P. B.; Christy, R. W. Optical Constants of the Noble Metals. *Phys. Rev. B* **1972**, *6*, 4370–4379.

- (42) Johnson, P. B.; Christy, R. W. Optical Constants of Transition Metals: Ti, V, Cr, Mn, Fe, Co, Ni, and Pd. Phys. Rev. B 1974, 9, 5056-5070.
- (43) Wu, Y.; Li, G.; Cherqui, C.; Bigelow, N. W.; Thakkar, N.; Masiello, D. J.; Camden, J. P.; Rack, P. D. Electron Energy Loss Spectroscopy Study of the Full Plasmonic Spectrum of Self-Assembled Au-Ag Alloy Nanoparticles: Unraveling Size, Composition, and Substrate Effects. ACS Photonics 2016, 3, 130-138.
- (44) Alexander, D. T. L.; Forrer, D.; Rossi, E.; Lidorikis, E.; Agnoli, S.; Bernasconi, G. D.; Butet, J.; Martin, O. J. F.; Amendola, V. Electronic Structure-Dependent Surface Plasmon Resonance in Single Au-Fe Nanoalloys. Nano Lett. 2019, 19, 5754-5761.
- (45) McKeown, J. T.; Roberts, N. A.; Fowlkes, J. D.; Wu, Y.; LaGrange, T.; Reed, B. W.; Campbell, G. H.; Rack, P. D. Real-Time Observation of Nanosecond Liquid-Phase Assembly of Nickel Nanoparticles via Pulsed-Laser Heating. Langmuir 2012, 28, 17168-17175.
- (46) Favazza, C.; Kalyanaraman, R.; Sureshkumar, R. Robust Nanopatterning by Laser-Induced Dewetting of Metal Nanofilms. Nanotechnology 2006, 17, 4229.
- (47) Wu, Y.; Fowlkes, J. D.; Rack, P. D. The Optical Properties of Cu-Ni Nanoparticles Produced via Pulsed Laser Dewetting of Ultrathin Films: The Effect of Nanoparticle Size and Composition on the Plasmon Response. J. Mater. Res. 2011, 26, 277-287.
- (48) Fowlkes, J. D.; Wu, Y.; Rack, P. D. Directed Assembly of Bimetallic Nanoparticles by Pulsed-Laser-Induced Dewetting: A Unique Time and Length Scale Regime. ACS Appl. Mater. Interfaces 2010, 2, 2153-2161.
- (49) Oh, Y.; Lee, J.; Lee, M. Fabrication of Ag-Au Bimetallic Nanoparticles by Laser-Induced Dewetting of Bilayer Films. Appl. Surf. Sci. 2018, 434, 1293-1299.
- (50) McKeown, J. T.; Wu, Y.; Fowlkes, J. D.; Rack, P. D.; Campbell, G. H. Simultaneous In-Situ Synthesis and Characterization of Co@Cu Core-Shell Nanoparticle Arrays. Adv. Mater. 2015, 27, 1060-1065.
- (51) Sachan, R.; Yadavali, S.; Shirato, N.; Krishna, H.; Ramos, V.; Duscher, G.; Pennycook, S. J.; Gangopadhyay, A. K.; Garcia, H.; Kalyanaraman, R. Self-Organized Bimetallic Ag-Co Nanoparticles with Tunable Localized Surface Plasmons Showing High Environmental Stability and Sensitivity. Nanotechnology 2012, 23, No. 275604.
- (52) Oh, Y.; Lee, J.; Lee, M. Fabrication of Ag-Au Bimetallic Nanoparticles by Laser-Induced Dewetting of Bilayer Films. Appl. Surf. Sci. 2018, 434, 1293-1299.
- (53) Allaire, R. H.; Dhakane, A.; Emery, R.; Ganesh, P.; Rack, P. D.; Kondic, L.; Cummings, L.; Fuentes-Cabrera, M. Surface, Interface, and Temperature Effects on the Phase Separation and Nanoparticle Self Assembly of Bi-Metallic Ni0.5Ag0.5: A Molecular Dynamics Study. Nanomaterials 2019, 9, 1040.
- (54) Zhang, C.; Dyck, O.; Garfinkel, D. A.; Stanford, M. G.; Belianinov, A. A.; Fowlkes, J. D.; Jesse, S.; Rack, P. D. Pulsed Laser-Assisted Helium Ion Nanomachining of Monolayer Graphene-Direct-Write Kirigami Patterns. Nanomaterials 2019, 9, No. E1394.

□ Recommended by ACS

All-Optical Manipulation of Magnetization in Ferromagnetic Thin Films Enhanced by Plasmonic Resonances

Feng Cheng, Yongmin Liu, et al.

JULY 29, 2020 NANO LETTERS

RFAD 🗹

Understanding Optomagnetic Interactions in Fe Nanowire-Au Nanoring Hybrid Structures Synthesized through Coaxial Lithography

Seung-Hoon Lee, Jae-Won Jang, et al.

MARCH 25, 2020

CHEMISTRY OF MATERIALS

READ **C**

Visualizing Electric and Magnetic Field Coupling in Au-Nanorod Trimer Structures via Stimulated Electron Energy Gain and Cathodoluminescence Spectroscopy...

David A. Garfinkel, Philip D. Rack, et al.

FEBRUARY 01, 2022

ACS APPLIED NANO MATERIALS

READ **C**

High Spin Polarization in Co₂FeSn Heusler Nanowires for Spintronics

Ladislav Galdun, Victor M. Prida, et al.

JULY 22, 2020

ACS APPLIED NANO MATERIALS

RFAD 🗹

Get More Suggestions >